Spatial and Temporal Variability in Tide-induced Icequake Activity at the Astrolabe Coastal Glacier, East Antarctica

Tifenn Le Bris[1], Guilhem Barruol[1], Florent Gimbert[1], Emmanuel Le Meur[1], Dimitri Zigone[2], Anuar Togaibekov[1], Denis Lombardi[3]

1. Univ. Grenoble Alpes, CNRS, INRAE, IRD, Grenoble INP, IGE, 38000 Grenoble, France
2. Université de Strasbourg/CNRS, Institut Terre et Environnement de Strasbourg, UMR7063, 67084 Strasbourg Cedex, France
3. SEISTREAM, Versailles, France

Corresponding author: Tifenn Le Bris (tifenn.le-bris@univ-grenoble-alpes.fr)

Key points:

1. Icequake activity over the grounding zone is modulated by tides, with peaks during mid-rising and mid-falling phases.
2. Short-scale spatio-temporal variations in icequake activity obtained from a dense array of seismic nodes outlines the grounding zone.
3. Cryoseismicity provides insights into the 3D dynamics of the grounding zone system as it undergoes tide-induced flexuring.

Abstract

The grounding zone (GZ) of a marine-terminating glacier, where ice transitions from grounded to floating, experiences strong mechanical changes, in particular in response to ocean tides. The spatial and temporal dynamics of these changes, however, remain poorly documented, as they require multi-scale observations capable of resolving internal ice deformation. Here we use multi-year and multi scale seismic observations to detect and locate icequakes resulting from the brittle deformation of the Astrolabe Glacier, an outlet glacier from East Antarctica (Terre Adélie). We find from automatic detection that seismicity strongly varies with tides and location of the sensors. At a

29   multi-kilometer scale, we observe and locate large-magnitude events associated with shear margins.

30   At smaller scale (few hundreds of meters), using a dense array of seismic nodes deployed across the

31   GZ, we capture numerous small-magnitude events whose occurrence is controlled by the GZ

32   geometry and dynamics. At rising tide, seismicity is dominant on the floating part of the glacier while

33   at falling tides, it is dominant over its grounded part. These short-scale spatio-temporal variations

34   lead us to propose a conceptual framework for the dynamics of icequake activity at the glacier GZ,

35   accounting for its three-dimensional tidal-induced bending and its confinement in a fjord. Our

36   findings highlight the value of dense seismic networks in capturing the high-resolution response of

37   outlet glaciers to tidal forces at their GZ.

38   **Plain Language Summary**

39   The Antarctic ice sheet naturally flows from its interior toward the oceans through ice shelves and

40   outlet glaciers, which form large floating ice tongues at the ocean surface. As glaciers transition from

41   grounded on the continent to floating on the ocean at their grounding zone (GZ), they are impacted

42   by the ocean effects, such as mechanical deformation caused by daily tides. Here, we present the

43   analysis of ice deformation at the GZ of the Astrolabe Glacier, in Terre Adélie, East Antarctica. This

44   analysis is based on data recorded by seismic instruments deployed on and around the glacier, on

45   land and at sea, from a few weeks to several years, with a particular focus on its GZ. We analyze

46   continuous seismic records to quantify the time and space occurrence of cryoseismic activity relative

47   to the GZ geometry and tides. We show that the ice flow is accommodated laterally by large

48   magnitude events along the lateral shear zones and that the tides are accommodated at the GZ by

49   numerous small magnitude icequakes occurring dominantly during mid-rising and mid-falling tides,

50   suggesting a complex three-dimensional bending of the floating tongue.

51   **1 Introduction**

52   Outlet glaciers in Antarctica and Greenland are at the forefront of global climate change (Jordan et

53   al., 2023). Their mechanical response at the ocean-continent transition influences ice sheet stability

54   and serves as a sensitive indicator of climate shifts. Monitoring their dynamics is key for accurate

55   model predictions of future sea level rise. Following the IPCC reports (IPCC Report, 2022),

56   international initiatives such as RINGS Action Group (2022) or INSTANT

57   (https://scar.org/science/research-programmes/instant) point the importance of better constraining

58   the past and present geometries of ice sheets and glaciers, particularly at their continent-ocean

59   transition (ice thickness, bedrock depth, grounding line and subglacial cavity geometry…). While the

60   grounding line is classically defined from large-scale satellite imagery as the linear boundary between

61   grounded and floating ice, local bedrock geometry can introduce small-scale complexities,

62   transforming this boundary into a broader area, referred to as the grounding zone (GZ). This

63   terminology will be used throughout the rest of this paper. The difficulty in apprehending the

64   behavior of outlet glaciers resides in the multiple thermal and mechanical interactions at the

65   different interfaces : at its basal and lateral boundaries where ice slides over the bedrock

66   (Weertman, 1957), at its front where it faces the ocean and sea-ice (Amundson et al., 2010;

67   Bartholomaus et al., 2015), and at its GZ; A major control on the dynamics of glaciers across their GZ

68   results from tide activity generating changes in sea surface height, inducing potential GZ horizontal

69   back and forth motions, depending on the bedrock topography, affecting the ice flux to the ocean

70   tides and the stability of the entire upstream basin (e.g., Pattyn, 2018; Rignot et al., 2011; Schoof,

71   2007).

72   The dynamics of Antarctic outlet glaciers GZ has been widely studied through remote sensing,

73   providing a large-scale picture of ice masses displacements (Friedl et al., 2020; Rignot et al., 2011),

74   sometimes complemented by ground GNSS measurements (King et al., 2010; Winberry et al., 2013).

75   However, these measurements only provide a surface-level perspective over extended time spans

76   (hours to days, even years), often lacking temporal continuity down to few seconds at which

77   processes may occur. Recent studies, however, succeeded to indirectly reach the daily tidal temporal

78   resolution by analyzing long-term remote sensing time-series and stacking observations to recreate

79   daily cycles (Freer et al., 2023; Rignot et al., 2024). As a complementary approach, cryoseismology

80   offers a valuable tool to gain insights into glaciers flow and deformation within the ice column—

81   from the surface to the bedrock — and over short spatial and temporal scales. Continuous recordings

82   of ice-related seismic activity enable the detection and location of seismic events with spatial

83   resolution down to a few meters and temporal variability ranging from seconds to seasons. This

84   approach provides a comprehensive view of the main underlying processes and external forces at

85   play, such as tides for coastal glaciers (e.g., Aster & Winberry, 2017; Podolskiy & Walter, 2016).

86   Seismic records from grounded glaciers are generally dominated by two main seismic activities. A

87   first group of low amplitude, repetitive and high frequency events is known to be induced by the

88   stick-slip motion at the ice-bedrock interface (e.g., Helmstetter et al., 2015; Lucas et al., 2023; Pirli et

89   al., 2018; Winberry et al., 2013; Zoet et al., 2012); a second, on which we focus the present study,

90   represents the primary - or at least the most frequent - source of seismicity, generating the largest

91   signals in glacier systems and widely accepted to result from ice brittle deformation. In

92   comprehensive overviews, Podolskiy & Walter (2016) followed by Aster & Winberry (2017)

93   referenced and synthesized early works on these so-called "icequakes" (Lewandowska and Teisseyre

94   1964; Neave & Savage, 1970; Osten-Woldenburg, 1990; Röthlisberg, 1955; Röthlisberger, 1972). In

95   recent years, subsequent researches have continued to build upon these studies and gained in

96   spatial resolution (e.g Hammer et al., 2015; Hudson et al., 2019; Kufner et al., 2023). For instance,

97   icequakes generated by the opening of crevasses have been successfully located to precisely map the

98   crevasse field of an Alpine glacier and its dynamics (Gimbert et al. 2021, Nanni et al. 2022). If

99   cryoseismicity has been in few cases described as induced by temperature variation (e.g.,Lombardi et

100 al., 2019), most events originate from complex time and space variations of stress, resulting from the

101 brittle behavior of ice as a response to flexuring (e.g., Hulbe et al., 2016), extension and shearing

102 regimes (e.g., Hudson et al., 2020). For coastal glaciers, the cyclic bending of the glacier floating

103 tongue under the ocean tidal modulation has been shown to generate such intense seismic activity

104 (Barruol et al., 2013; Cooley et al., 2019; Fromm et al., 2023; Lombardi et al., 2016).

105 Seismic records in GZ areas depict recurring patterns in response to tides. At the Ekström Ice Shelf,

106 dominant local and regional icequakes were found to mainly occur during rising tides, and proposed

107 to be associated with opening of cavities at the bottom of the glacier, driven by the upward bending

108 of the floating tongue (Fromm et al., 2023; Hammer et al., 2015). Near the Roi Baudouin Ice Shelf,

109 Lombardi et al. (2016) identified periodic seismic activity correlated with tide-induced bending,

110 particularly during rising and high tides, that they potentially linked to basal crevassing. By contrast, a

111 study focused on Ice Stream C from Anandakrishnan & Alley (1997), with a 6-week deployment at a

112 distance of 85 km from the GZ, revealed basal seismicity mostly activated just before the minimum

113 tide. In the vicinity of the Mertz Glacier in East Antarctica and of the Bowdoin Glacier in West

114 Greenland, Barruol et al. (2013) and Podolskiy et al. (2016) highlighted icequake seismicity to have a

115 clear tidal modulation with a dominant peak of seismic activity at falling tide, i.e., during the

116 downward bending of the glacier floating tongue and a weaker activity during tide rising phases. In

117 addition to the double-peak diurnal oscillation, Podolskiy et al. (2016) also found an horizontal

118 acceleration of the glacier at falling tide, interpreted as its longitudinal stretching. Minowa et al.

119 (2019) suggested that the extension movement associated to the bending during falling tide could

120 generate crevasse opening at the surface, leading to higher icequake activity. However, there is no

121 consensus on whether this bending generates seismic energy mainly during rising and/or falling tides,

122 and whether it results from basal or surface crevassing, or both. Additionally, the relative importance

123 of the various mechanisms occurring at different places of the glacier remains uncertain, including

124 basal slip events, lateral shear zones events, and surface extensional or compressional events caused

125 by the glacier horizontal acceleration or deceleration.

126 The present study analyzes the cryoseismic activity of the Astrolabe Glacier in Terre Adélie, East

127 Antarctica by combining large-scale and long-term with small-scale and short-term seismic networks.

128 This strategy allows us to investigate the distribution of events by magnitude and location, and to

129   understand how these are influenced by the instrumental setup, the 3D geometry of the glacier GZ

130   and lateral shear zones.

131   **2 Data and Methods**

132   2.1 Study site

133   The Astrolabe Glacier (66°41' S, 140°05' E) is located in Terre Adélie, East Antarctica, near the

134   Dumont d'Urville (DDU) French polar base (Fig. 1). The floating tongue of this outlet glacier is

135   approximately 4 km wide and 10 km long and is fed by a basin extending more than 200 km into the

136   continent (Mouginot et al., 2014). In the studied area, the ice flows at a rate of up to 500 m/year (Le

137   Meur et al., 2014; Provost et al., 2024). Compared to its eastward neighbours Cook and Mertz

138   glaciers, the catchment area of the Astrolabe Glacier is relatively small (~1500 km² against 307 741

139   km² for the Cook basin and 84 543km² for the Mertz basin, see Rignot et al. (2013)). Its small size and

140   easy access from the nearby DDU station both provide a unique opportunity to cover the entire

141   system from its grounded zone to its ocean terminus with a limited number of instruments that can

142   be deployed with reasonable logistical support.

143   The floating part of the Astrolabe glacier is laterally constrained within a fjord with valley walls 500 to

144   600 m deep, covered by grounded stable ice, as imaged by radar surveys (Le Meur et al., 2014) and

145   bathymetric surveys offshore (Beaman et al., 2011). These features create strong shear zones on

146   both sides of the glacier, accommodating the relative displacement between the glacier, the bedrock,

147   and the surrounding stable ice, as evidenced by satellite imagery (e.g., Provost et al., 2024). The

148   floating tongue thickness is estimated to be around 600 m at the GZ, progressively thinning to about

149   300 m at its terminus on the ocean (Le Meur et al., 2014). In front of the terminus, the fjord

150   bathymetry extends deeper than 1000 m (Beaman et al., 2011), resulting in a large subglacial cavity

151   beneath the floating ice tongue, prone to ocean penetration and ice basal melting. The glacier front

152   is directly exposed to ocean swells (when there is no sea ice in summer), storms and tides.

153
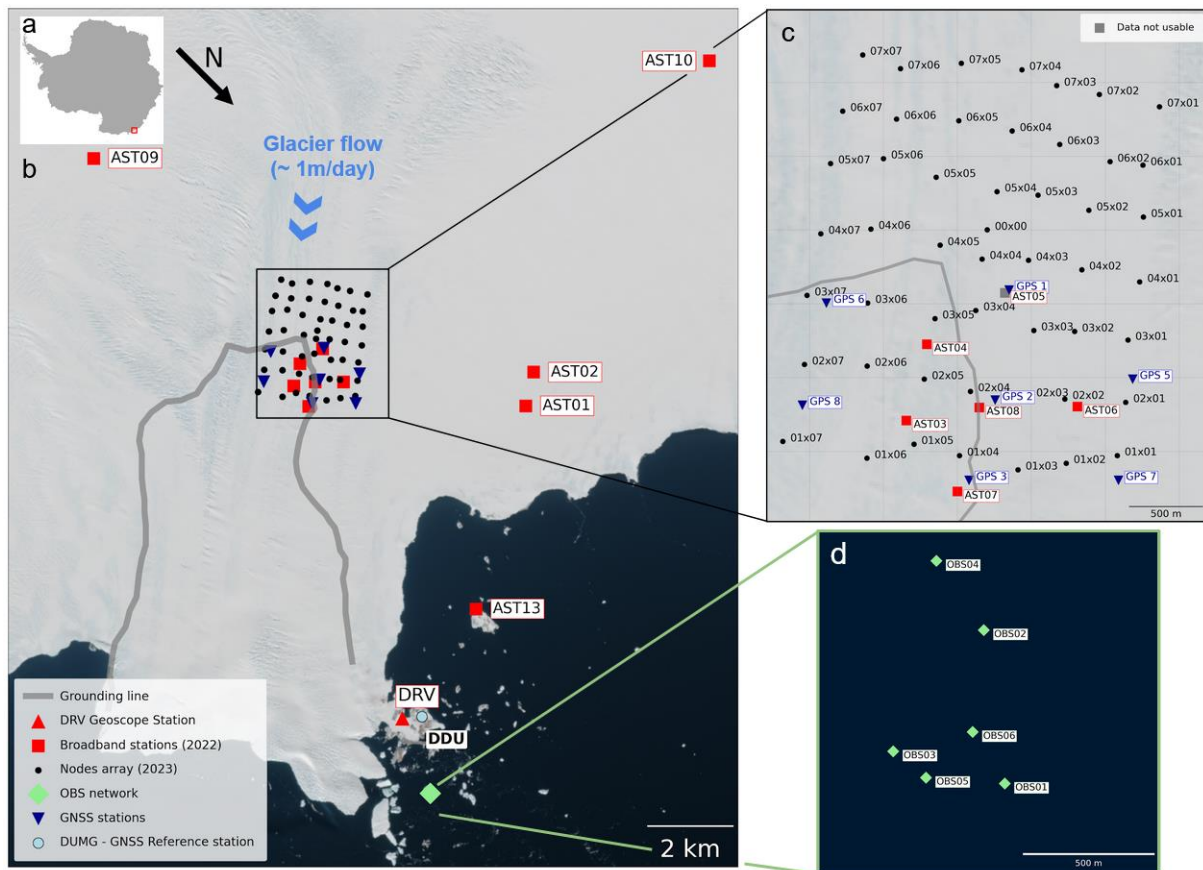
Figure 1: Map of the deployments on and around the Astrolabe glacier. (a) Study site location in East Antarctica. (b) Astrolabe glacier with locations of the seismic and GNSS stations (symbols explained in the insert), in the neighborhood of the Dumont d'Urville (DDU) French Polar base. Satellite image is from Sentinel 2. Grey line represents the grounding line inferred from geodetic GNSS analyzes from Le Meur et al. (2014). (c) Zoom on the instrumented GZ area of the glacier with location of the GNSS stations (blue triangles), the broadband seismic network deployed for 3 weeks in January 2022 (red squares) and the seismic nodes deployed for 3 weeks in January 2023 (black dots). (d) zoom on the coastal area where Ocean Bottom Seismometers (OBSs) have been deployed in 2022-2023. See details on instruments deployment in Table S1 (Supp. Info.).

2.2 Seismological deployments

With support from the French Polar Institute, we deployed a network of seismometers on and around the glacier from 2020 to 2024. This included both terrestrial and ocean-bottom seismometers (OBS) respectively on land and at sea (Fig. 1 and Table S1. of Supp. Info. for details). Starting in 2022, broadband stations were deployed during several years around the glacier on grounded (stable) ice or on rocky outcrops. For these stations, the sampling rate has been set to 100 Hz. We also use the permanent Geoscope station DRV at the DDU base, operational since 1986 (Leroy et al., 2023; Institut de physique du globe de Paris (IPGP) and École et Observatoire des Sciences de la Terre de

172   Strasbourg (EOST), 1982) and set at 20 Hz sampling frequency since 1999, allowing long-term

173   seismological investigation over several decades (Grob et al., 2011; Stutzmann et al., 2009).

174   In January 2022, a temporary network of 6 broadband seismometers was deployed for 3 weeks in the

175   grounding zone area of the glacier (Fig. 1), all recording at 200 Hz. Due to melt-induced sensor tilting,

176   data from AST05 were unusable. Simultaneously, five short period [4.5- 300] Hz and intermediate

177   band [0.1-100] Hz OBS were deployed in front of the glacier terminus for 2 to 3 weeks in January

178   2022. Two of these were redeployed in early February 2022 for a full year, including a wintering

179   under the sea ice.

180   In January 2023, we enhanced event detection and structural imaging by deploying a network of 50

181   three-component seismic nodes in the GZ (Fig. 1). Spaced 300-400 m apart, the seismic nodes

182   covered ~2x2 km² and recorded continuously at 500 Hz for about three weeks. In the present paper,

183   data analysis focuses on January 14-24, 2023, after which stormy weather caused considerably

184   decreased data quality.

185   2.3 Complementary deployments

186   To complement the seismological observations, we gather GNSS data from 9 autonomous GPS

187   beacons that have been recording over the GZ area almost continuously since 2010 (Le Meur et al.,

188   2014). In our 2022 and 2023 instrumental deployments, some seismic stations were co-located with

189   the GNSS stations (Fig. 1c). For those, the sampling rate was set to 30s during the seismic survey

190   period to provide better resolution of vertical and horizontal ice motion. During the remaining time

191   of the year, the stations recorded one sample every 30s during each two-hour session occurring

192   three times every day. GPS data processing details are available in Text S1 (Supp. Info.).

193   We evaluate and quantify tides using the PM36S MarArgos automatic tide gauge called DUMON,

194   installed at the DDU base. This station measures local tide height with a 2-minute sampling rate

195   (NIVMER/ROSAME project, Calzas et al., 1992). Data are transmitted in real time via Argos, and have

196   been used to perform frequency spectral harmonic analysis of the signal (Pawlowicz et al., 2002), to

197   extract phases and amplitudes of the tidal components, and to compare seismic activity with tidal

198   dynamics.

199   2.4 Icequake detection

200   We identify icequakes within continuous seismic records and analyze their occurrence using a

201   systematic event triggering algorithm based on the STA/LTA (short-term average/long-term average)

202   method (Allen, 1978; Lesage, 2009), well adapted for detecting impulsive events. Fig. 2a displays a

203   representative 8-min long recording from the AST03 broadband seismic station situated on the

204   Astrolabe GZ. Among the diverse signals, icequakes are easily identifiable by their impulsive arrivals

205   and the lack of clear distinction between seismic phases. We use the following parameters: STA is set

206   to 0.5s, LTA to 5s, trigger threshold On and Off to 5 and 2, respectively. These values were

207   determined by minimizing missed events and false detections based on visual comparisons between

208   detections and phase arrivals observed in the waveforms (1 hour of record screened per day). We

209   apply these parameters for all the stations. By bandpass filtering the data, we narrow down the used

210   frequency band to [5-40] Hz, where most icequake energy is concentrated (see spectrogram in Fig.

211   2b). The dashed grey lines in Fig. 2a indicate the icequakes detected over the 8 min recording

212   example. Fig. 2c and 2d present an example of the trigger on (red) and trigger off (blue) thresholds

213   over a single event and its corresponding STA/LTA ratio curve. In our analysis, events with duration

214   smaller than 0.4 seconds are set aside as they are under-represented and might originate from false

215   detections.

216   Despite the limitations inherent to the method (i.e. false detections, missing events), we expect

217   some consistency in the error rates for each station, ensuring a rather robust relative comparison

218   between them. Systematic detections performed at each station display a significant number of

219   events with considerable hourly variability (typically ranging between few tenths and 500

220   events/hour). From the catalogues of detections obtained for each station, we compute time series

221   of icequake occurrences every hour, which is long enough to gather sufficient statistics while short

222   enough to investigate diurnal modulation.

223   The systematic use of the STA/LTA detection algorithm also provides an event duration for each

224   detected icequake (Fig. 2c). From this measured duration, we attribute an event magnitude of

225   duration (Md) using the empirical relationship expressed as *Md = -0.9 + 2log(d)* with *d* the event

226   duration (Lee et al., 1972). While this empirical relationship is commonly used in earthquake studies,

227   we acknowledge limitations in our present situation, mainly due to difficulties in precisely identifying

228   event start and end times (due to the complex waveform of icequakes), but also due to icequakes

229   not necessarily obeying similar laws to earthquakes. The duration magnitudes thus should not be

230   interpreted in an absolute sense but rather as a proxy for relative comparison between events.

231

232
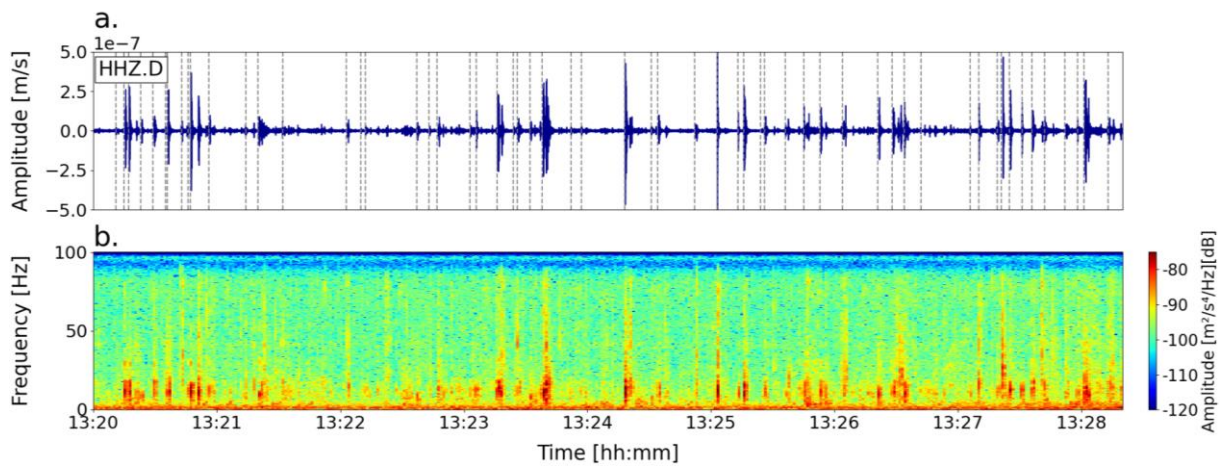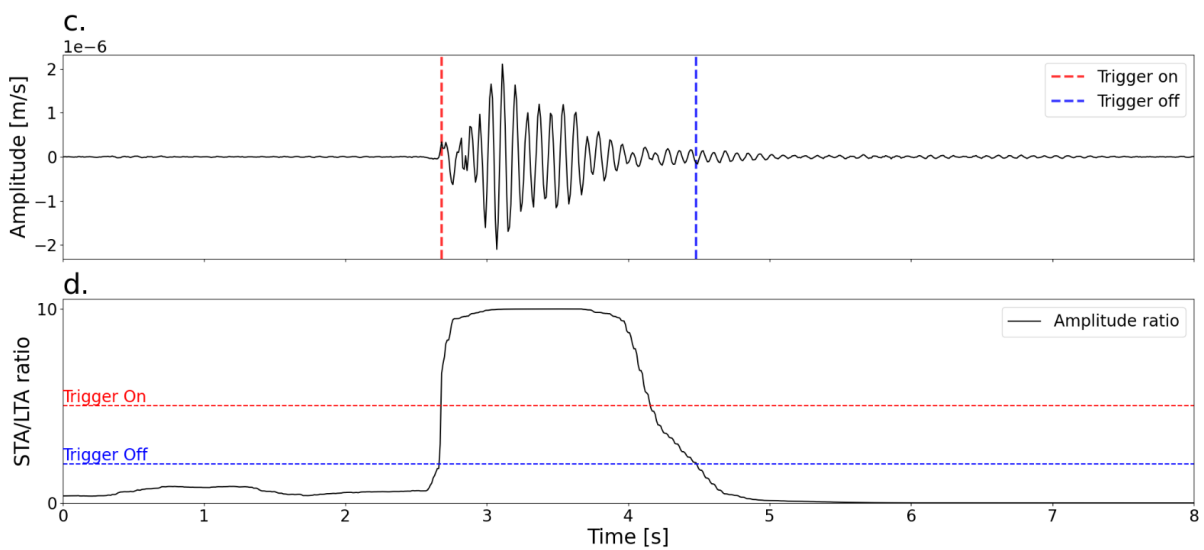
Figure 2: Seismic waveforms and icequakes detection. (a) Seismic waveform and (b) spectrogram of
eight minutes of recording on the Z component of station AST08, located on the GZ of the Astrolabe
glacier (Fig. 1), on Jan. 20, 2022. Data sampled at 200 Hz are bandpass filtered between 5 and 100 Hz.
Seismic event detections are indicated by timestamps (grey dotted lines) for events detected by the
STA/ LTA algorithm. (c) Zoom on 8s of records (vertical, HHZ component) showing a single detection
with the trigger On (red) and Off (blue) timestamps. (d) Corresponding STA/LTA amplitude ratio curve
with the amplitude ratio trigger On (red) and trigger Off (blue) thresholds.

2.5 Icequake location

To evaluate icequake locations we use the dense seismic array, and adopt two distinct strategies. For
large magnitude events, which generate a coherent wavefield all across the seismic node array, we
apply Match Field Processing (MFP) as described and detailed in other studies (Chmiel et al., 2019;
Gimbert et al., 2021; Nanni et al., 2022). This method recursively matches observed seismic field
phase delays with a modeled one using a point-like source and a frequency-domain Green's function,

246   which depends on four parameters: the source spatial coordinates (x, y, z) and the medium

247   homogeneous phase velocity (c). For each time window, chosen to approximate the seismic wave

248   travel time across the array, the best source likelihood is determined by minimizing the relative

249   difference between observed and modeled phase delays. The MFP output is normalized between 0

250   and 1, with higher values indicating a better match and greater confidence in the source location.

251   Instead of using a computationally expensive multi-dimensional grid search, we employ a

252   minimization algorithm based on the downhill simplex method (Nelder-Mead optimization) as

253   described by Nelder & Mead (1965) and Lagarias et al. (1998). To maximize the likelihood of

254   identifying dominant sources within 2-second time windows, we initiate the algorithm from 13

255   starting points distributed over a 1500 × 1500 m² area centered on the node array, reducing

256   azimuthal bias. All localizations from these 13 minimizations are evaluated based on their MFP

257   output values. The algorithm is allowed to detect multiple sources within the same time window,

258   selecting those with MFP outputs above 0.2 to ensure meaningful source localization.

259   For the numerous small magnitude events, which are higher frequency and which do not generate

260   coherent waves across the array, MFP turns out unsuccessful. Instead of looking at individual event

261   location, we thus map sources only in a statistical sense, either by mapping icequake occurrence

262   detected at each node sensor, or by mapping the number of seismic nodes that detected a given

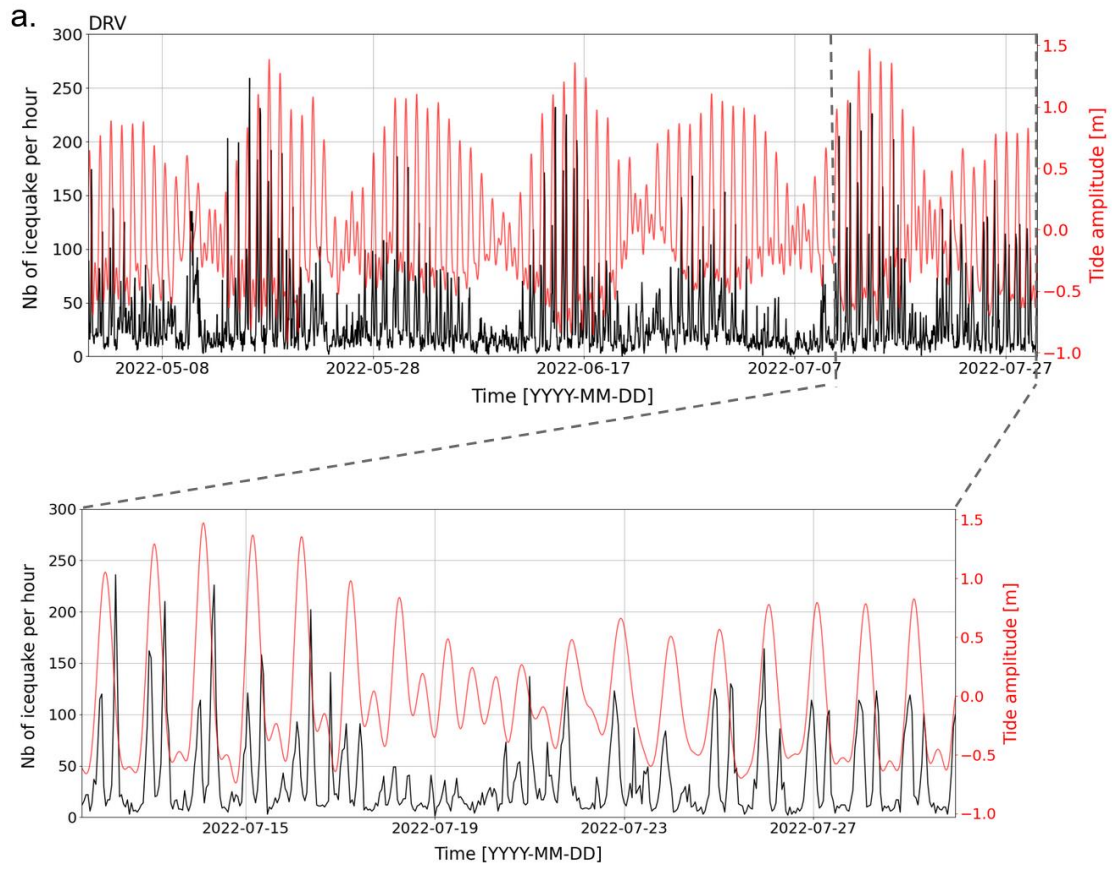263   event, which turn to be extremely informative.

264   **3 Results**

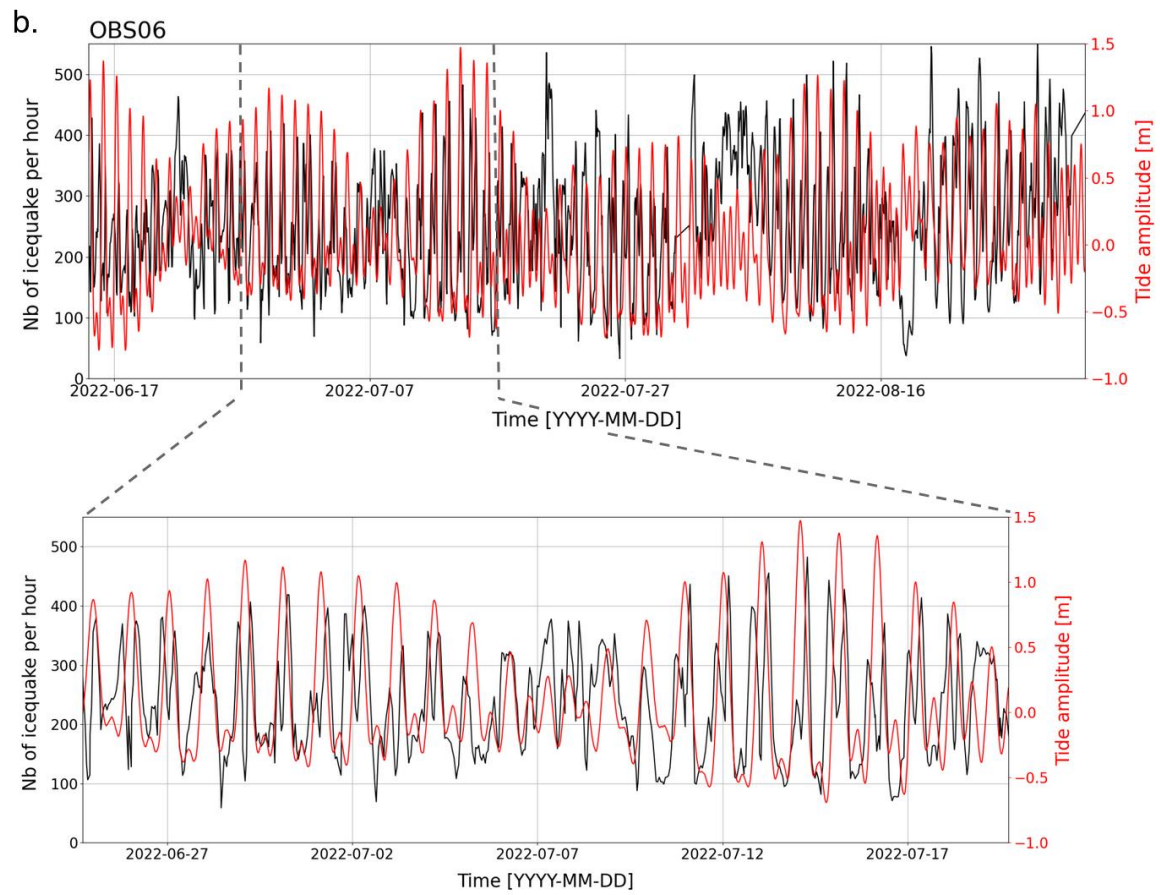265   3.1 Long-range and long-term tide-modulated seismicity

266   We first characterize the relationship between icequake activity and ocean tides using data from two

267   stations located at a large distance from the GZ (>10 km), on a rocky outcrop (DRV) and on the ocean

268   bottom (OBS06) and running over the course of the year 2022. The 3 months event detection on the

269   DRV 20 Hz vertical data channel (Fig. 3a) displays a distinct modulation in icequake hourly occurrence

270   across successive spring and neap tide cycles, exhibiting event counts ranging from 10 to over 200

271   events per hour. Zooming on a shorter time scale, we observe double peaks for diurnal cycles,

272   aligning with rising and falling tides (Fig. 3a). During periods with high tide amplitude, we often

273   observe a stronger activity during the falling tide phase (from July 07, 2022 to July 15, 2022 on Fig.

274   3b). Although this pattern is recurring across consecutive tide cycles, it does not consistently appear

275   throughout the entire analyzed time series. At station OBS06 deployed at sea close to the glacier

276   front, we also observe a clear correlation of the icequake occurrence with the tidal amplitudes across

277   spring and neap tide cycles (Fig. 3b), showcasing an increase in icequake activity during high tide

278   periods. On average, the rate of icequake occurrences surpasses that observed at the DRV station,

279   varying between 100 and 400 events per hour. Additionally, we identify distinct double peaks of

280   seismicity during diurnal cycles, also aligning with rising and falling tides (zoom Fig. 3b). Although the

281   two peaks of seismicity mainly exhibit similar amplitudes, we punctually find a slightly higher activity

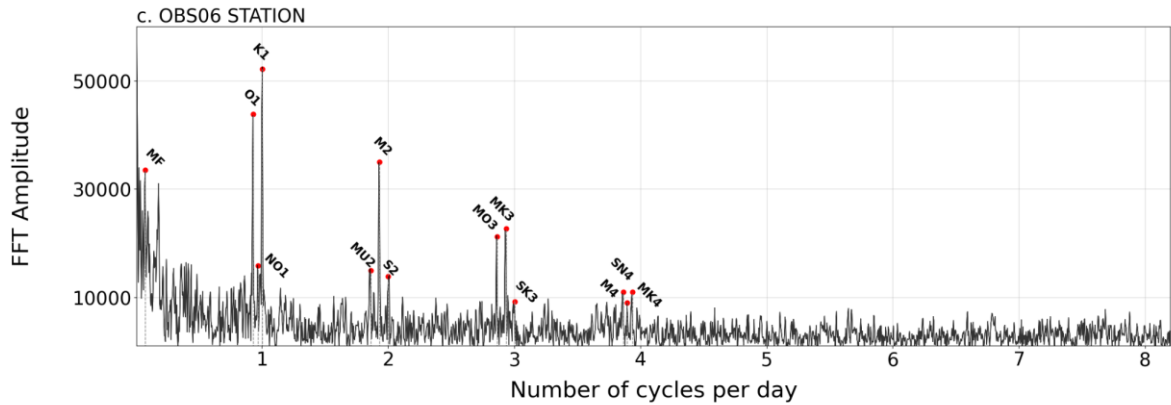282   during the falling tide similar to what is observed at DRV station.

283   We perform a Fast Fourier Transform (FFT) spectral analysis on the hourly icequake occurrence time

284   series and compare it with tidal harmonics issued from tide gauge data (Fig. 4). The timeseries, of

285   same duration for both stations (i.e., 9 months), allow to compare spectral amplitudes and are long

286   enough to properly resolve periods of up to one month. Tide gauge measurements mostly show

287   diurnal and semidiurnal tidal cycles, with smaller amplitude peaks for monthly, fortnightly and

288   terdiurnal cycles (Fig. 4a). These cycles stand out very clearly for FFT spectra of DRV and OBS06

289   stations (Fig. 4b and 4c). OBS06 frequency peak amplitudes are twice as strong as those at DRV, and

290   the noise level is also higher. This difference with DRV may be due to OBS06 proximity to the glacier

291   terminus and the local submarine conditions, respectively increasing both signal amplitude and

292   noise. The monthly and fortnightly, as well as diurnal and semidiurnal, tidal modulations of the

293   cryoseismicity are well-documented in several studies focused on ice displacement and icequake

294   activity (Aðalgeirsdóttir et al., 2008; Barruol et al., 2013; Bindschadler et al., 2003; Fromm et al.,

295   2023; Gudmundsson, 2007; Minowa et al., 2019; Murray et al., 2007), reflecting that ice deformation

296   at the GZ is controlled by glacier displacement and tidal amplitudes. Sensitivity to higher tidal cycle

297   frequencies (3 and 4 cycles per day - cpd for both stations and up to 8 cpd for DRV) have also been

298   observed in other seismic or GNSS datasets (Barruol et al., 2013; Fromm et al., 2023; Minowa et al.,

299   2019). While the 4 cpd peak can be explained by the double seismicity peak at mid-rising and mid-

300   falling tides, the terdiurnal peak at 3 cpd and higher frequency peaks remain open to interpretation.

301   They could reflect tidal overharmonics (generated by non-linear interactions of the main tidal

302   harmonics as a result of ice/ocean interactions) as proposed by Fromm et al. (2023) or alternatively

303   result from anelastic processes at the GZ as suggested by Pedley et al. (1986).

a.

304

b.

305

306 **Figure 3:** Examples of icequake occurrence (black curves, number of icequakes per hour) compared

307 to the local tide amplitudes measured at the DUMON tide gauge at Dumont d'Urville base (red

308 curves, tide amplitude in m). (a) Top: for seismic station DRV over 4 months (May-Aug 2022).

309 Bottom: Zoom of DRV over a 20-day period in July 2022. (b) Top: for the ocean bottom seismometer

310 OBS06 deployed on the seafloor near the glacier terminus (see location Fig. 1). Bottom: Zoom of

311 OBS06 over a 20-day period in July 2022.

312

c. OBS06 STATION

Figure 4: Tides and cryoseismic spectra. (a) Fast Fourier Transform (FFT) of the tide amplitude measured at the DUMON tide gauge installed at the Dumont d'Urville station, (b) FFT of the icequake hourly occurrence at the Geoscope DRV seismological station (over 9 months) and (c) FFT of the icequake hourly occurrence at the ocean bottom station OBS06 (over 9 months). Seismic frequency peaks are well correlated with tide harmonics, as calculated from t-tides software (Pawlowicz et al., 2002) and marked by vertical dotted lines with red dots at the extremity: Fortnightly (MSF), diurnal (2Q1,Q1,01,NO1,K1,J1,001), semidiurnal (EPS2,MU2,N2,M2,L2,S2,ETA2), terdiurnal (MO3,M3,MK3,SK3) and quarterdiurnal (MN4,M4,SN4,MS4,MK4,S4,SK4) temporal tidal cycles.

a. Grounding zone (AST03)

324

325
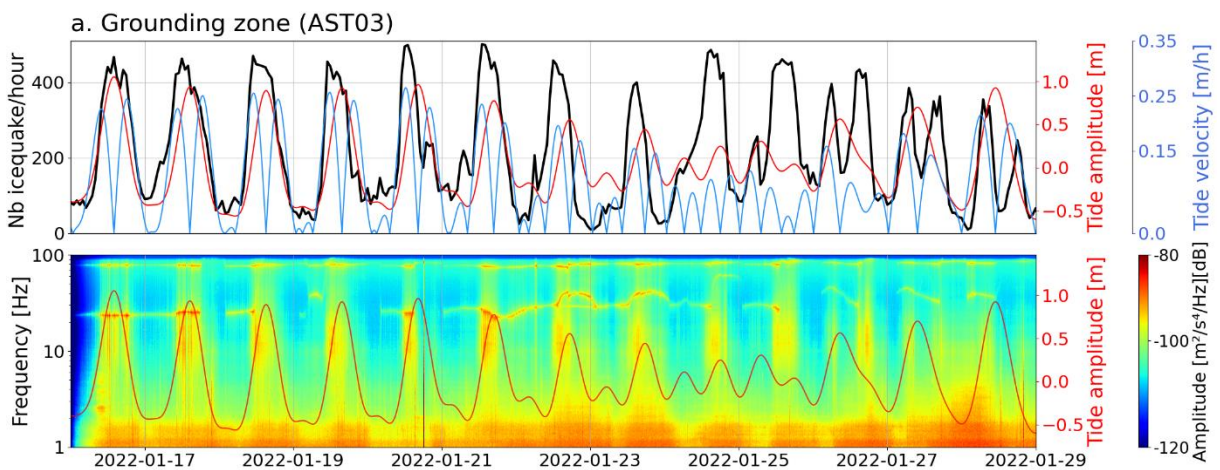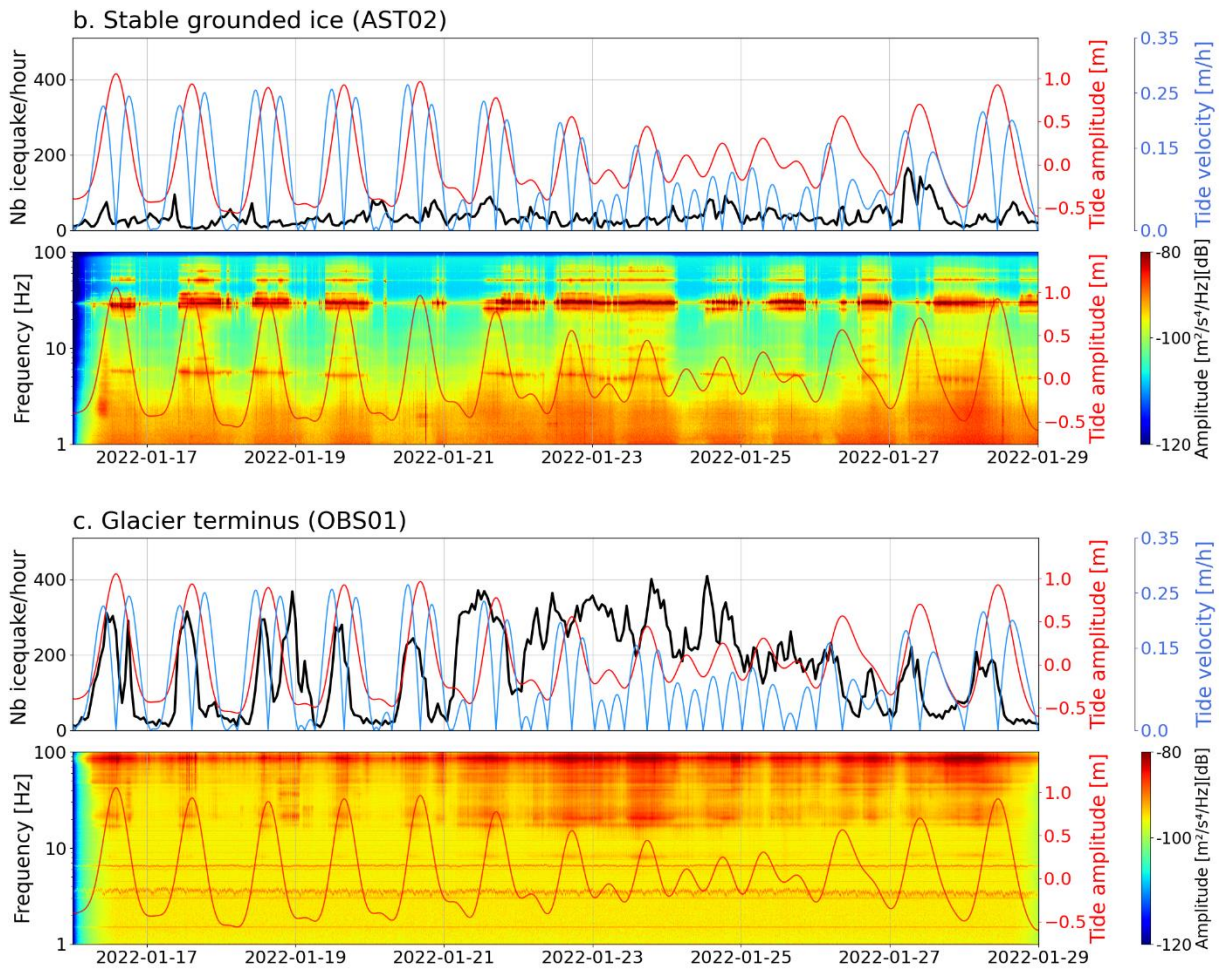
Figure 5: Tide amplitudes, tide velocity, icequake rate and spectral energy at few examples of

terrestrial and ocean bottom seismic stations for the period January 16 to 29, 2022. Top plots:

Number of detected seismic events (black curve) per hour compared with tide amplitude (red curve)

and tide vertical velocity (blue curve) for (a) seismic stations AST03 on floating ice, (b) AST02 on

stable grounded ice and (c) OBS01 on the seafloor near the glacier terminus. Bottom plots:

Spectrograms of seismic energy alongside tide amplitude (red curves) for the same seismic stations.

Spectrograms are generated using the Logarithmic Power Spectral Density (LPSD) method on the

vertical (Z) component of the data, with 10-minute windows covering the 1-100 Hz frequency range.

Welch's method is applied on 10-second segments within each window, and the mean power is

computed and converted to decibels (dB). For broadband stations, the instrumental response is

removed. This correction was not available for the OBS station. The distinct monochromatic spectral

lines at ~30 Hz and higher frequencies at AST02 are likely caused by wind-induced vibrations

affecting the cables holding the station solar panels.

3.2 Tidal modulation of icequake occurrence around the grounding zone

340 While the seismic observations performed at a large distance to the GZ highlight similar global
341 patterns, we observe differences in the phasing between the tides and the icequake peak
342 occurrences at stations located closer to the GZ (Fig. 5). There, we detect a large number of events
343 (e.g. 450 and 300 events/hr for AST03 and OBS01, respectively) clearly modulated by the tides with
344 peak seismicity mostly occurring at highest tide amplitude, such as before Jan. 21, 2022 for AST03 on
345 Fig. 5a. We can occasionally observe double peaks of seismicity (well visible after Jan. 27, 2022 for
346 AST03 on Fig. 5a) that match double peaks in absolute tide vertical velocity, (calculated as the norm
347 of the time derivative of sea surface height). For the OBSs at sea, we mainly observe double peaks of
348 seismicity also happening when the tide vertical velocity is the highest (mid-rising and mid-falling
349 tide), particularly well visible Fig. 3b and prominent at rising tide before Jan 21, 2022 on Fig. 5c. A
350 distinct pattern is observed for stations AST02 (Fig. 5b) and AST01 (Fig. S1, Supp. Info.), both located
351 on the stable, grounded ice (see Fig. 1), where we detect only a small number of events (generally
352 less than 100 events/h), without any clear correlation with the ocean tides. This different behavior
353 can be explained by sensors being primarily sensitive to the local seismicity, i.e. from the lateral
354 shear zone of the glacier around 1 km away, and much less sensitive to events from the GZ, likely too
355 far away (around 5 km). Dominant tide-modulated seismicity thus occurs locally near the GZ, but is
356 not detected at larger distances.

357 Spectrograms from stations located on the GZ (e.g., AST03, Fig. 5a) follow the same tidal variations,
358 with energy primarily released during both rising and falling tides. The tidally modulated increase of
359 energy is particularly strong between 10 Hz and 20 Hz, matching with the frequency band where
360 icequake energy is most prominent. At station AST02 installed on the stable grounded ice,
361 spectrogram also shows daily seismic energy modulation (Fig. 5b) which is likely dominated by the
362 wind daily variation, and not by the icequake signal which is found to be very low in this area. The
363 spectrogram from the OBS (Fig. 5c) shows strong energy levels above 20 Hz during high tide,
364 especially between the 16th and 22nd of January.

365 Distinct temporalities in seismicity across seismic stations also reflect in distinct event magnitude
366 distributions (see few selected stations is shown in Fig. 6), among which two distinct regimes
367 emerge. Stations on the glacier (e.g., AST03, AST08) and near the glacier terminus (e.g., OBS01)
368 exhibit similar icequake duration and magnitude distributions, with duration completeness typically
369 observed between 0.5 and 0.7 seconds (corresponding magnitudes completeness between -1.5 and -
370 1.2) consistent with observations of Barruol et al. (2013) and Podolskiy et al. (2016). Stations located
371 around the glacier, at a larger distance to its GZ (e.g., AST02, DRV), display a notably different
372 distribution, characterized by a completeness shifted towards longer durations, around 1 second
373 (magnitude of completeness around -0.9). The strong deficit in short duration/magnitude events

374 recorded at these sites indicates that they do not catch the icequake activity from the GZ, which is

375 clearly dominated by much smaller magnitude events. This confirms that small icequakes dominate

376 the signal in the active area of the glacier, causing distinct seismicity patterns and tidal signatures.
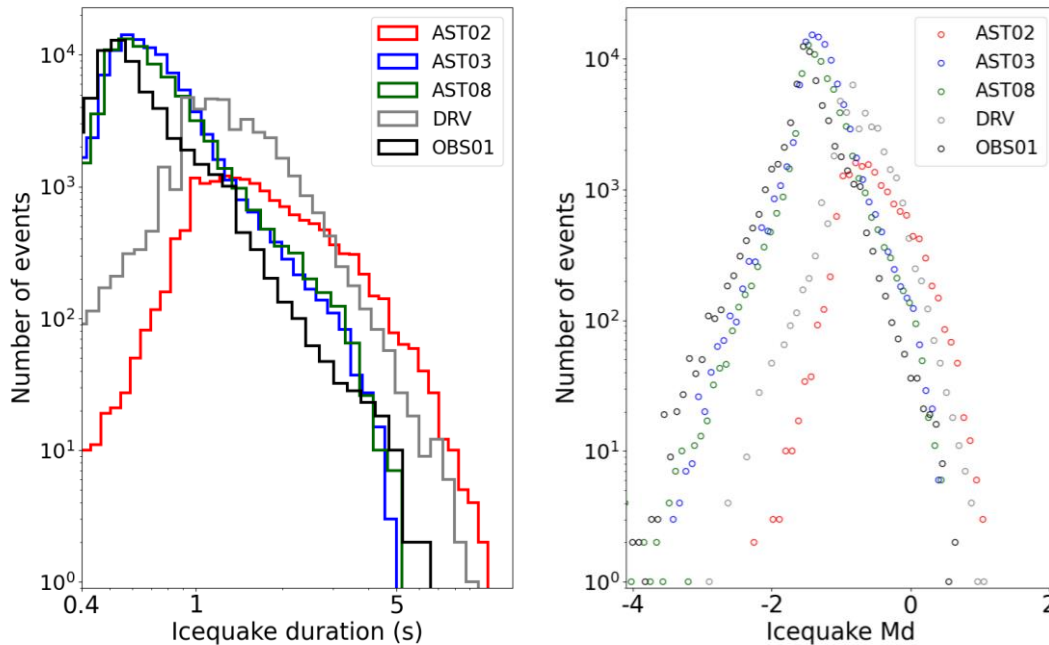
377

378 **Figure 6:** Icequake duration (left) and magnitude distribution (right) for stations AST02 (red), AST03

379 (blue), AST08 (green), DRV (grey) and OBS01 (black). X-axis and y-axis are in logarithmic scale.

380 3.3 Small scale spatial and temporal icequake activity within the grounding zone area

381 3.3.1. Source locations of small events

382 In order to explore with high resolution the temporal and spatial variability of small magnitude

383 icequake activity at the Astrolabe Glacier GZ, we use the data acquired in January 2023 by 50 seismic

384 nodes (Fig. 1b and c). In Fig. 7a we present an overlay of the 50 icequakes hourly occurrence time

385 series (in black), superimposed with the measured tide amplitude (in red) and the derived tide

386 vertical velocity (in blue), complemented by a zoom over 4 days for a clearer view (Fig. 7b).

387 Consistent with our observations from the 2022 seismic broadband network (Section 3.2, Fig. 5), we

388 observe a clear period of seismic quiescence during low tides and peaks of seismic activity

389 concomitant with high tides. Additionally, we observe double peaks in icequake occurrence during

390 cycles with larger tide amplitudes, which are well correlated with peaks in tidal velocities.
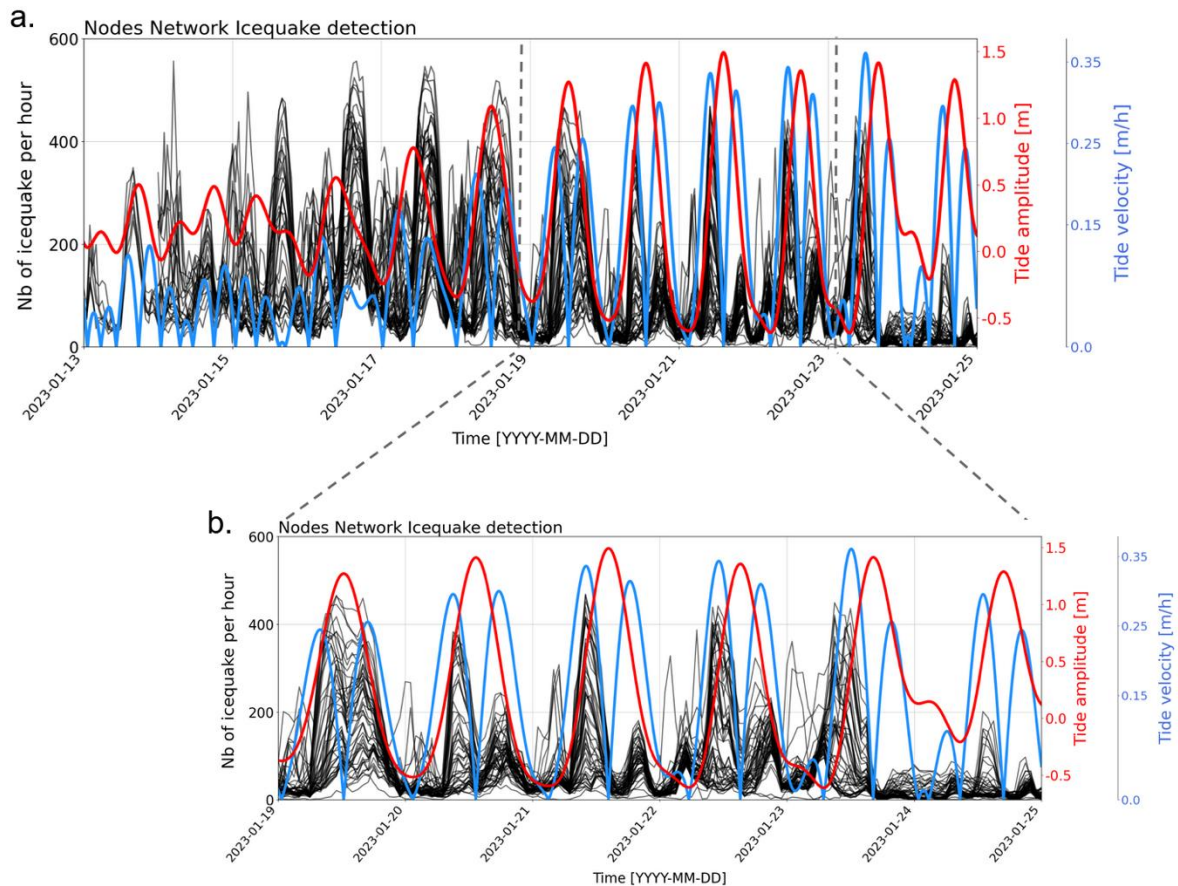
Figure 7: Icequakes occurrence at the seismic nodes. (a) Time series of icequakes hourly occurrence measured at each of the 50 seismic nodes (black curves), along with the sea surface height (red curve) and the derived tide vertical velocity (blue curve) on the Astrolabe Glacier GZ during the period Jan 13-25, 2023. (b) Zoom on the period Jan 19-25, 2024. The network deployment was completed on Jan 16, 2023. STA/LTA parameters: sta = 0.5s, lta = 5s, ThrOn = 5, ThrOff = 2.

Interestingly, we observe that the number of detected events strongly varies across the various seismic nodes, with peaks lower than 100 events per hour to peaks higher than 400 events per hour. When examining the average detected seismicity at each node (Fig. 8a), these variations reveal a coherent spatial structure strikingly outlining the GZ. Regions of floating ice northeast of the GZ (indicated by stronger reddish colors) exhibit higher seismic activity than the western and southwestern parts of the network. These seismic observations match well with the GNSS-derived vertical motions (see grey squares), which show large values in the northeast corner, where the glacier is floating and seismicity is high, and weaker vertical motions in the southern and western regions, where the glacier is likely grounded and seismicity is low.

In order to further investigate the fine-scale spatial pattern of icequake occurrence, we count the number of stations detecting any given event (using a 2-second time window). This allows us to make

maps of the number of events detected by a given number of stations. This is illustrated Fig. 8b and c
by the number of events detected by less than 10 and more than 40 stations. Events detected by 10
stations or less (Fig. 8b) are clearly concentrated near the GZ in the eastern part of the network,
corresponding to the glacier floating sector. In contrast, events detected by more than 40 stations
(Fig. 8c) show an even distribution across the network, indicating that fewer but larger-magnitude
events are detected. The statistics of events by bins of number of sensors are summarized in Table S2
(Supp. Info.). The majority of events (63%) are detected by less than 10 stations or between 11 and
20 stations (25%), while only a small percentage (2%) are detected by more than 40 stations. This
detection pattern aligns well with the magnitude distribution in Fig. 6, where small magnitude events
dominate and are mostly not coherently observed across the whole array, despite its restricted
spatial scale of few kilometers.
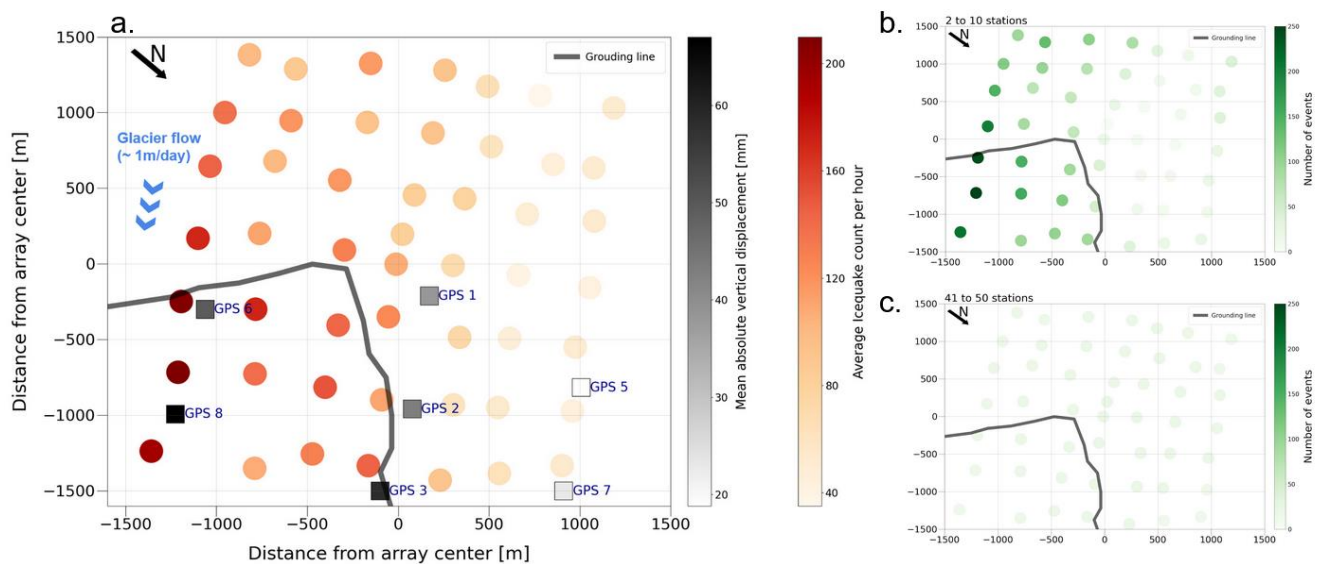
Figure 8: (a) Map of the hourly average icequake activity during the period Jan 14-24, 2023 (color-
coded in red, indicating the average icequakes count per hour) recorded at each station of the
seismic node network (circles), together with the average vertical ice displacements shown as
squares filled with a level of grey indicating the mean value in mm measured by the GNSS stations.
Continuous grey line represents the grounding line (GL) inferred from GPS observations (Le Meur et
al., 2014). (b) Map of the number of icequakes detected by less than 10 stations (color-coded in
green), for one day (Jan 17, 2023) representative of an "average" tide cycle (i.e. with a mean tide
height of +/- 0.5m). (c) Map of the number of events seen by more than 40 stations for the same day.
Each station is colour-coded based on the number of icequakes detected in the corresponding
category.

430   The temporal distribution of event number between rising and falling tides also follows a specific

431   spatial pattern. To illustrate this, we analyze the variance of icequake occurrence at each station as

432   the difference between the average hourly icequake number during rising and falling tides, divided

433   by the average number during rising tides (Fig. 9). During rising tides, icequake activity increases in

434   the floating part of the network (reddish dots in Fig. 9), while during falling tides, activity rises in the

435   grounded part (blueish dots in Fig. 9), particularly in the western and southern sectors. In both cases,

436   the variance of icequake occurrence can reach up to 40%, indicating significant shift of the seismic

437   activity at a fine spatio-temporal scale, from the floating area at rising tides toward the grounded

438   area at falling tides. Despite such spatial map of icequakes occurrence, we are unable to individually

439   locate them because most events are recorded by too few stations and exhibit strong waveforms

440   variations likely caused by surface crevassing. In the following section, we will address this by using

441   the Match Field Processing (MFP) technique to localize the fraction of larger magnitude events that

442   are coherently detected across the entire array.

443
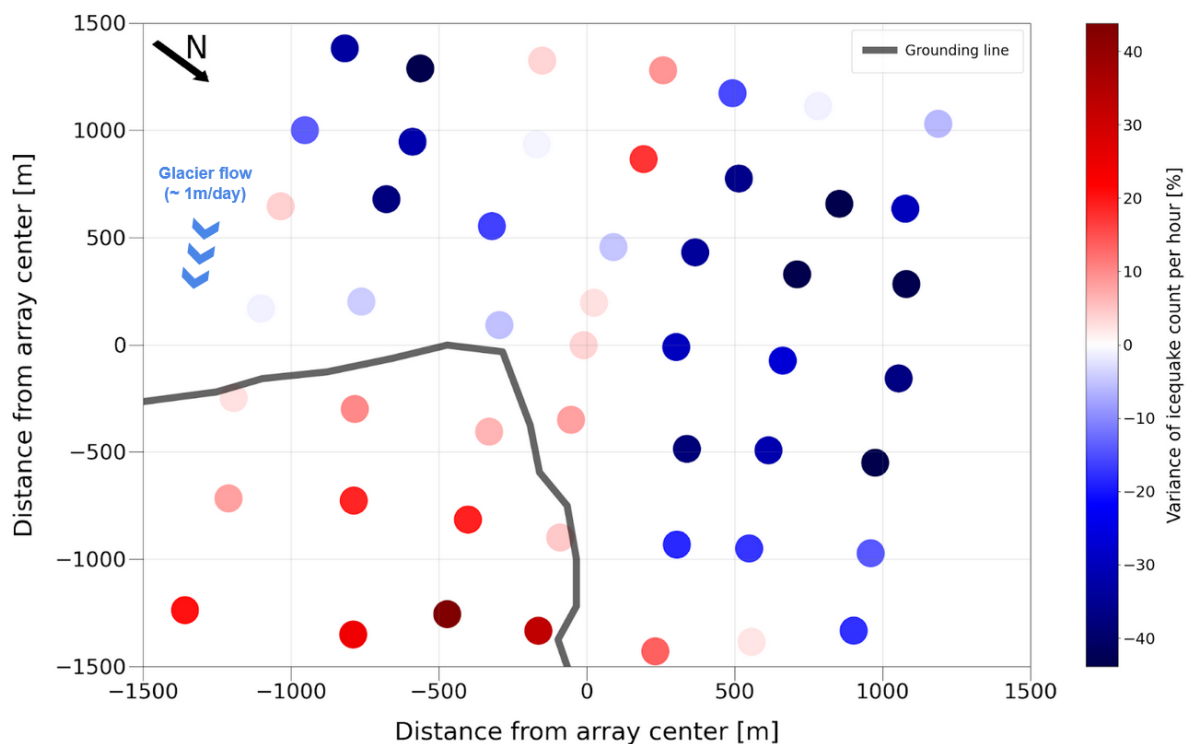
444

445   **Figure 9:** Map summarising the icequake variance (in %). Reddish colors indicate dominant icequake

446   activity during rising tides whereas blueish colors indicate dominant icequake activity during falling

447   tides. Continuous grey line represents the grounding line (GL) inferred from GPS observations (Le

448   Meur et al., 2014).

3.3.2 Seismic source locations for large events

By using the Match Field Processing (MFP) method described in section 2.5, we locate events over the selected period Jan 17, 2023 to Jan 24, 2023 (Fig. 10). The frequency range where MFP can be applied is conditioned by subwavelength spatial sampling, which, for an average sensor spacing of around 350 meters and surface wave velocities on the order of 1600 m/s, corresponds to an upper limit frequency of about 3 Hz. Meanwhile, signals below 1 Hz may be contaminated by the ocean-induced secondary microseisms, which are not of interest here. Thus, we apply the MFP in the [1-3] Hz frequency band, for which only the largest icequakes are observed, and for which seismic waves are not significantly attenuated across the 3-km scale of the seismic array, such that spatial seismic waveform coherency is preserved. We find that these large magnitude events are dominantly clustered on the lateral shear margins and in the floating part of the node array, thus exhibiting a similar pattern that the smaller seismicity shown in Fig. 8. We also evidence a population of deeper events distributed over the area, including a small linear cluster of events located over a section of the GZ border, that could correspond to brittle deformation at the base of the glacier related to opening of basal crevasses during the tide-induced bending of the glacier. Also consistent with observations regarding the small seismicity in Fig. 8, the largest seismicity shows little activity in south-western part of the array, and seismicity is also modulated by the tides although we identify no trend between rising and falling tides.

467
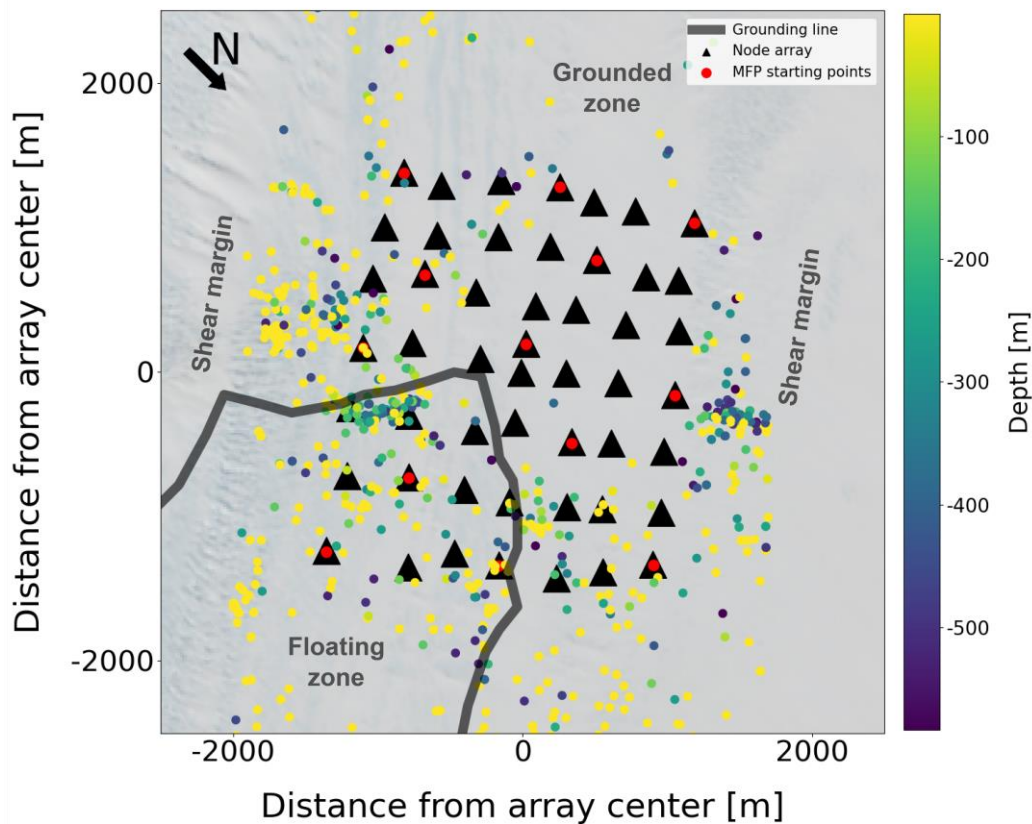
Figure 10: Map of seismic sources located using MFP analysis applied to the seismic node array. Black
triangles mark the positions of the seismic nodes, while red dots represent the starting points for the
MFP computations. Continuous grey line represents the grounding line (GL) inferred from GPS
observations (Le Meur et al., 2014). Seismic sources are shown as colored dots, with colors
representing their depth.

4 DISCUSSION

4.1 Glacier dynamics and icequakes tidal modulation

The occurrence of icequakes, which indicates brittle failure of the ice, provides insight into how
stress from the glacier floating tongue flexure is accommodated during tidal cycles. The presence of
two distinct phases of seismicity—associated with rising and falling tides—illustrates the complex
response of glacier bending to ocean activity. The vertical motion of the floating tongue, whether
upwards or downwards, alters the state of stress and subsequently the strain state to accommodate

481   the glacier flexure at its GZ. At low tide systematically, and at high tide more sporadically, we observe

482   a clear reduction of the seismic activity, even though the bending of the floating tongue is at its

483   maximum compared to an expected floating equilibrium position. On the other hand, during rising

484   and falling tides when strain rate is the highest, seismicity is observed to be the highest. Generally,

485   the intensity of the flexure-related icequake activity correlates well with the tide magnitude.

486   However, some stations show persistent seismic activity despite small tide amplitudes, indicating

487   possible nonlinear interactions between ocean tides and non-elastic processes at the GZ. This

488   highlights the complex relationship between tides and glacier dynamics already observed at other

489   glaciers (e.g., Fromm et al., 2023). At certain stations on the glacier floating part, high seismic activity

490   at high tide (e.g., AST03 on Jan. 18 and 19, 2022, as shown in Fig. 5a) suggests additional glacier

491   acceleration effects. This may contribute to longitudinal extension observed by remote sensing

492   (Provost et al., 2024) and could be accommodated by numerous low-magnitude icequakes, as noted

493   by Minowa et al. (2019).

494   4.2 Small versus large seismicity

495   Our seismic measurements reveal a wide range of icequake activity. Small magnitude events

496   (maximum magnitude around 1.2, magnitude of completeness around -1.5, see Fig. 6) have

497   frequency contents dominating in the range of 5-40 Hz and can occur up to 5000 times per day at

498   some stations. They exhibit hardly discernible seismic phases and their waveforms and arrival times

499   are strongly affected along their traveling path - likely by surface heterogeneities induced by open

500   crevasses but also due to attenuation. These events are widespread across the node network but are

501   most prominent on the glacier floating tongue. They exhibit clear tidal modulation, peaking at mid-

502   rising and mid-falling tides, with the seismic activity at mid-rising tide being predominantly observed

503   on the floating tongue while the seismic activity at mid-falling tide is concentrated in the (partly)

504   grounded area upstream of the GZ. Large magnitude and low frequency events, with frequency

505   ranging down to 1 Hz, can occur up to 200 times per day, and are well detected using Match Field

506   Processing (MFP) analysis. These large events are primarily located outside the seismic node

507   network, often at shallow depths (<100m), particularly in the lateral shear zones where the ice

508   deforms relative to stable ice or bedrock (see yellow stars in Fig. 11b and c). They are also observed

509   on the floating part of the network, suggesting significant deformation possibly linked to longitudinal

510   glacier acceleration. They are clearly absent from the grounded part of the node network, where

511   deformation is dominated by small magnitude events accommodating the glacier flexure. These

512   findings highlight the power of dense seismic network in discriminating various seismic sources (GZ

513   and shear margins). In addition to GZ networks, future deployments on outlet glaciers should

514   therefore include dense arrays at the shear margins, with the aim of identifying and locating its

515   seismicity to better discriminate the one at the GZ. Additionally, in order to properly locate the small

516   seismicity around the GZ, one should reduce the inter station distance to increase the aliasing

517   threshold to higher frequencies, allowing then to look into smaller magnitude events. In a case such

518   as the Astrolabe Glacier, this would require having a dense array with average inter-station distance

519   around or below 100m over the GZ.

520   4.3 Icequake activity from 2D to 3D GZ geometries

521   Our analysis demonstrates the benefit of high-resolution seismic observations for revealing the

522   three-dimensional (3D) nature of the GZ. For a hypothetical two-dimensional (2D) GZ, downward

523   bending of the glacier should occur at falling tides as illustrated in Fig. 11a. This bending would

524   primarily result in Mode I extension, opening cracks and crevasses near the surface above the GZ

525   (blue star, Fig. 11a), as described by Hulbe et al. (2016). In contrast, rising tides would cause the

526   floating tongue to move upward, reducing bending at the GZ with cracks and crevasses closing

527   aseismically while new flexure and seismic crevassing are expected to develop slightly downstream

528   (red star, Fig. 11a), as proposed by Rack et al. (2017). The offset between icequake activity during

529   falling and rising tides, related to the glacier curvature and ice thickness at the GZ, aligns with our

530   observations: more icequakes occur on the floating tongue during rising tides, and more on the GZ

531   during falling tides (Fig. 9). In addition to this 2D picture, we expect that the 3D geometry of the

532   Astrolabe Glacier also plays a role, given that the glacier is 3 to 4 km wide, about 0.6 km thick, and

533   laterally confined within a fjord with steep walls. Our measurements, along with the node network

534   over the U-shaped GZ (Fig. 1), indicate that the glacier is grounded beneath both its southern and

535   western sections. This is confirmed by stronger icequake activity at stations on the floating part of

536   the glacier (Figs. 7 and 8) and differing seismic activity patterns between rising and falling tides (Fig.

537   9). During rising tides, the glacier lateral boundaries may restrict vertical displacement, causing

538   transverse bulging of the floating part of the glacier and Mode I extension near the surface on both

539   lateral sides (red stars, Fig. 11b). This effect is sampled by the western part of our node network. At

540   falling tides, surface crack closure is mostly seismically silent. We propose that both 2D and 3D

541   processes could explain the two distinct peaks in seismicity, which reflect surface brittle deformation

542   and spatial variations in icequake activity relative to the GZ during different tide phases. For a more

543   detailed understanding of the 3D flexure and associated seismicity, further modeling of stress

544   distribution across complex GZ systems under tidal oscillations would be required, including complex

545   bedrock topography and realistic tide activity.
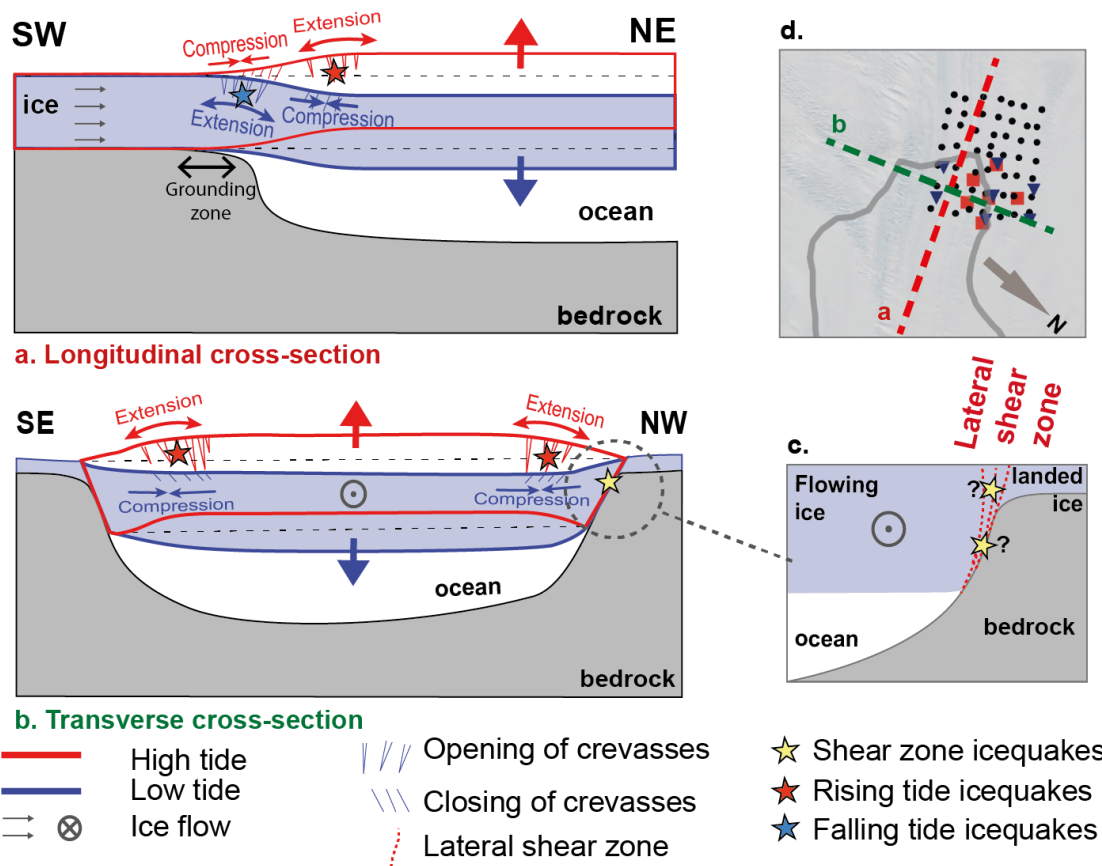
Figure 11: Schematic cartoons illustrating the possible origin of the surface icequakes observed on the Astrolabe Glacier: a.) Icequakes generated by the longitudinal bending of the glacier in response to tidal vertical variations (cross-section a in red), with the blue star indicating the extrados crevasse opening during falling tides and the red star the extrados crevassing at rising tides. b.) Cartoon of the transverse bending of the glacier during rising tides (cross-section b in green). c.) Large-magnitude icequakes primarily associated with the lateral shear zones (yellow stars) accommodating the relative displacement of the glacier horizontal flow compared to the stationary ice at the surface or bedrock at greater depths. d.) Position of the longitudinal (red) and transverse (green) schematic cross sections.

4.4 Dense seismic arrays for efficient monitoring of the GZ position

Our observations indicate that the timing at which we observe maximum icequake activity at a given site is strongly dependent on the sensor location relative to the GZ. Seismicity on the GZ is of particularly small magnitude and thus not regionally detectable, while seismicity on the shear margins is higher in magnitude and thus may dominate records at stations farther away from the GZ. This relative location may control if the icequake detection peak occurs either during rising, falling, or both tide periods. Despite limitations in instrument number and fieldwork logistics, our setup on the

563   Astrolabe Glacier demonstrates that a well-distributed, km-scale network with sufficient station

564   density can effectively capture the diverse signals generated by the glacier complex structure and

565   dynamics. Initial observations with a limited number of broadband stations already provided a great

566   overview of key patterns, such as very low seismic activity at low tides and increased seismic strain

567   accommodation during rising and falling tides. A denser network of seismic nodes on the GZ proved,

568   however, much higher resolution in both time and space, allowing detailed monitoring of the glacier

569   response to tidal movements within its complex bedrock geometry and, in our case, even allows to

570   resolve the GZ position. Indeed, by deploying a dense network of seismic nodes over a marine-

571   terminating glacier GZ, we effectively delineate and monitor this critical boundary through its

572   cryoseismicity. Our observations reveal how seismic activity reflects glacier deformation at the GZ in

573   response to tidal forces, highlighting significant strain in regions where the glacier transitions from

574   grounded to floating. This refined understanding of the GZ location and dynamics is achievable only

575   with a dense network of seismic stations, as sparse or remote setups would not capture the fine-

576   scale variations of seismicity associated with tidal cycles. In the studied case of the Astrolabe Glacier,

577   the kilometer-scale experiment has proven to be sufficient to observe with a good resolution the

578   variations in the icequake activity during tidal cycles in the different areas of the GZ (floating versus

579   grounded). This setup is particularly well-suited for glaciers of moderate size. Deployments on much

580   larger glaciers would require a rough estimate of the GZ position to ensure that a dense seismic array

581   spans the transition zone, which can extend several tens of kilometers for some glaciers. To maintain

582   high resolution within the array while keeping inter-station distances relatively small (a few hundred

583   meters), more sensors would be needed, thus presenting both logistical and instrumental challenges.

584

585   **5 Conclusions**

586   By deploying broadband and short-period seismometers and a dense seismic array over periods

587   ranging from weeks to years at the grounding zone (GZ) of an Antarctic outlet glacier, we quantified

588   icequake activity at this critical frontier where continental ice reaches the ocean. While diurnal and

589   semidiurnal tidal periods dominate in the seismic patterns, we also observe significant effects at

590   fortnightly, monthly, terdiurnal, and quarterdiurnal cycles, indicating complex interactions between

591   tides, the floating ice tongue, and the underlying ocean. We observe very low seismicity at low tide

592   and peaks during rising and falling phases, often correlated with tide vertical velocities. From the

593   dense seismic array, we detect and locate large magnitude cryoseismic events, primarily induced by

594   deformation along the glacier lateral shear margins. Our detections also reveal numerous small-

595   magnitude events in the vicinity of the grounding zone, strongly influenced by tidal amplitudes and

596 GZ geometry. This latter seismicity is found to be more intense on the floating part of the glacier near
597 the GZ, suggesting that small, numerous icequakes accommodate its tide-induced bending. We
598 propose that the complex icequake patterns may be explained by the successive flexure and bulging
599 of the glacier confined within a fjord, in response to falling and rising tides, respectively. Finally, the
600 dense seismic array covering a large part of the GZ enables us to capture short-scale spatio-temporal
601 variations in icequake activity reflecting its outline. Such precise monitoring of the GZ will be of great
602 importance in characterizing its potential retreat induced by the changing climate, threatening the
603 future stability of the upstream ice sheet basin.

604

638

Data availability statement

References

652

653 Aðalgeirsdóttir, G., Smith, A. M., Murray, T., King, M. A., Makinson, K., Nicholls, K. W., & Behar, A. E.

654   (2008). Tidal influence on Rutford Ice Stream, West Antarctica: observations of surface flow

655   and basal processes from closely spaced GPS and passive seismic stations. *Journal of*

656   *Glaciology*, *54*(187), 715–724. https://doi.org/10.3189/002214308786570872

657 Allen, R. V. (1978). Automatic earthquake recognition and timing from single traces. *Bulletin of the*

658   *Seismological Society of America*, *68*(5), 1521–1532.

659   https://doi.org/10.1785/BSSA0680051521

660 Amundson, J. M., Fahnestock, M., Truffer, M., Brown, J., Lüthi, M. P., & Motyka, R. J. (2010). Ice

661   mélange dynamics and implications for terminus stability, Jakobshavn Isbræ, Greenland.

662   *Journal of Geophysical Research: Earth Surface*, *115*(F1).

663   https://doi.org/10.1029/2009JF001405

664 Anandakrishnan, S., & Alley, R. B. (1997). Tidal forcing of basal seismicity of ice stream C, West

665   Antarctica, observed far inland. *Journal of Geophysical Research: Solid Earth*, *102*(B7),

666   15183–15196. https://doi.org/10.1029/97JB01073

667 Aster, R. C., & Winberry, J. P. (2017). Glacial seismology. *Reports on Progress in Physics. Physical*

668   *Society (Great Britain)*, *80*(12), 126801. https://doi.org/10.1088/1361-6633/aa8473

669 Barruol, G., Cordier, E., Bascou, J., Fontaine, F. R., Legrésy, B., & Lescarmontier, L. (2013). Tide-

670   induced microseismicity in the Mertz glacier grounding area, East Antarctica. *Geophysical*

671   *Research Letters*, *40*(20), 5412–5416. https://doi.org/10.1002/2013GL057814

672 Bartholomaus, T. C., Larsen, C. F., West, M. E., O'Neel, S., Pettit, E. C., & Truffer, M. (2015). Tidal and

673   seasonal variations in calving flux observed with passive seismology. *Journal of Geophysical*

674   *Research: Earth Surface*, *120*(11), 2318–2337. https://doi.org/10.1002/2015JF003641

675 Beaman, R. J., O'Brien, P. E., Post, A. L., & Santis, L. D. (2011). A new high-resolution bathymetry

676   model for the Terre Adélie and George V continental margin, East Antarctica. *Antarctic*

677   *Science*, *23*(1), 95–103. https://doi.org/10.1017/S095410201000074X

678 Bindschadler, R. A., King, M. A., Alley, R. B., Anandakrishnan, S., & Padman, L. (2003). Tidally

679   Controlled Stick-Slip Discharge of a West Antarctic Ice Stream, *301*.

680 Calzas M., Techine P., Testut L. (1992) NIVMER, https://doi.org/10.18142/135

681 Chmiel, M., Roux, P., & Bardainne, T. (2019). High-sensitivity microseismic monitoring: Automatic

682   detection and localization of subsurface noise sources using matched-field processing and

683   dense patch arrays. *Geophysics*. https://doi.org/10.1190/geo2018-0537.1

684 Cooley, J., Winberry, P., Koutnik, M., & Conway, H. (2019). Tidal and spatial variability of flow speed

685   and seismicity near the grounding zone of Beardmore Glacier, Antarctica. *Annals of*

Glaciology, *60*(79), 37–44. https://doi.org/10.1017/aog.2019.14

Freer, B. I. D., Marsh, O. J., Hogg, A. E., Fricker, H. A., & Padman, L. (2023). Modes of Antarctic tidal grounding line migration revealed by Ice, Cloud, and land Elevation Satellite-2 (ICESat-2) laser altimetry. *The Cryosphere*, *17*(9), 4079–4101. https://doi.org/10.5194/tc-17-4079-2023

Friedl, P., Weiser, F., Fluhrer, A., & Braun, M. H. (2020). Remote sensing of glacier and ice sheet grounding lines: A review. *Earth-Science Reviews*, *201*, 102948. https://doi.org/10.1016/j.earscirev.2019.102948

Fromm, T., Schlindwein, V., Helm, V., & Fofonova, V. (2023). Observing tidal effects on the dynamics of the Ekström Ice Shelf with focus on quarterdiurnal and terdiurnal periods. *Journal of Glaciology*, 1–11. https://doi.org/10.1017/jog.2023.4

Gimbert, F., Nanni, U., Roux, P., Helmstetter, A., Garambois, S., Lecointre, A., et al. (2021). A Multi-Physics Experiment with a Temporary Dense Seismic Array on the Argentière Glacier, French Alps: The RESOLVE Project. *Seismological Research Letters*, *92*(2A), 1185–1201. https://doi.org/10.1785/0220200280

Grob, M., Maggi, A., & Stutzmann, E. (2011). Observations of the seasonality of the Antarctic microseismic signal, and its association to sea ice variability. *Geophysical Research Letters*, *38*(11). https://doi.org/10.1029/2011GL047525

Gudmundsson, G. H. (2007). Tides and the flow of Rutford Ice Stream, West Antarctica. *Journal of Geophysical Research: Earth Surface*, *112*(F4). https://doi.org/10.1029/2006JF000731

Hammer, C., Ohrnberger, M., & Schlindwein, V. (2015). Pattern of cryospheric seismic events observed at Ekström Ice Shelf, Antarctica. *Geophysical Research Letters*, *42*(10), 3936–3943. https://doi.org/10.1002/2015GL064029

Helmstetter, A., Nicolas, B., Comon, P., & Gay, M. (2015). Basal icequakes recorded beneath an Alpine glacier (Glacier d'Argentière, Mont Blanc, France): Evidence for stick-slip motion? *Journal of Geophysical Research: Earth Surface*, *120*(3), 379–401. https://doi.org/10.1002/2014JF003288

Hudson, T. S., Brisbourne, A. M., Walter, F., Gräff, D., White, R. S., & Smith, A. M. (2020). Icequake Source Mechanisms for Studying Glacial Sliding. *Journal of Geophysical Research: Earth Surface*, *125*(11), e2020JF005627. https://doi.org/10.1029/2020JF005627

Hudson, T. S., Smith, J., Brisbourne, A. M., & White, R. S. (2019). Automated detection of basal icequakes and discrimination from surface crevassing. *Annals of Glaciology*, *60*(79), 167–181. https://doi.org/10.1017/aog.2019.18

Hulbe, C. L., Klinger, M., Masterson, M., Catania, G., Cruikshank, K., & Bugni, A. (2016). Tidal bending and strand cracks at the Kamb Ice Stream grounding line, West Antarctica. *Journal of Glaciology*, *62*(235), 816–824. https://doi.org/10.1017/jog.2016.74

721 IPCC Report. (2022). *The Ocean and Cryosphere in a Changing Climate: Special Report of the*

722 *Intergovernmental Panel on Climate Change*. Cambridge: Cambridge University Press.

723 https://doi.org/10.1017/9781009157964

724 Institut de physique du globe de Paris (IPGP) and Ecole et Observatoire des Sciences de la Terre de

725 Strasbourg (EOST). (1982). *GEOSCOPE, French global network of broad band seismic stations*.

726 Institut de physique du globe de Paris (IPGP), Université de Paris.

727 https://doi.org/10.18715/GEOSCOPE.G

728 Jordan, J. R., Miles, B. W. J., Gudmundsson, G. H., Jamieson, S. S. R., Jenkins, A., & Stokes, C. R.

729 (2023). Increased warm water intrusions could cause mass loss in East Antarctica during the

730 next 200 years. *Nature Communications*, *14*(1), 1825. https://doi.org/10.1038/s41467-023-

731 37553-2

732 King, M. A., Altamimi, Z., Boehm, J., Bos, M., Dach, R., Elosegui, P., et al. (2010). Improved Constraints

733 on Models of Glacial Isostatic Adjustment: A Review of the Contribution of Ground-Based

734 Geodetic Observations. *Surveys in Geophysics*, *31*(5), 465–507.

735 https://doi.org/10.1007/s10712-010-9100-4

736 Kufner, S.-K., Wookey, J., Brisbourne, A. M., Martín, C., Hudson, T. S., Kendall, J.-M., & Smith, A. M.

737 (2023). Strongly depth-dependent ice fabric in a fast-flowing Antarctic ice stream revealed

738 with icequake observations. *Journal of Geophysical Research: Earth Surface*, *128*(3).

739 https://doi.org/10.1029/2022JF006853

740 Lagarias, J. C., Reeds, J. A., Wright, M. H., & Wright, P. E. (1998). Convergence Properties of the

741 Nelder--Mead Simplex Method in Low Dimensions. *SIAM Journal on Optimization*, *9*(1), 112–

742 147. https://doi.org/10.1137/S1052623496303470

743 Le Meur, E., Sacchettini, M., Garambois, S., Berthier, E., Drouet, A. S., Durand, G., et al. (2014). Two

744 independent methods for mapping the grounding line of an outlet glacier – an example from

745 the Astrolabe Glacier, Terre Adélie, Antarctica. *The Cryosphere*, *8*(4), 1331–1346.

746 https://doi.org/10.5194/tc-8-1331-2014

747 Lee, W. H. K., Bennett, R. E., & Meagher, K. L. (1972). *A method of estimating magnitude of local*

748 *earthquakes from signal duration* (Open-File Report). Menlo Park, Calif.: U.S. Geol. Surv.

749 Leroy, N., Vallée, M., Zigone, D., Romanowicz, B., Stutzmann, E., Maggi, A., et al. (2023). GEOSCOPE

750 Network: 40 Yr of Global Broadband Seismic Data. *Seismological Research Letters*.

751 https://doi.org/10.1785/0220230176

752 Lesage, P. (2009). Interactive Matlab software for the analysis of seismic volcanic signals. *Computers*

753 *& Geosciences*, *35*(10), 2137–2144. https://doi.org/10.1016/j.cageo.2009.01.010

754 Lewandowska, H., & Teisseyre, R. (1964). Investigations of the ice microtremors on Spitsbergen in

755 1962. *Biul Inf Komisji Wypraw Geof PAN*, *37*, 1-5.

756   Lombardi, D., Benoit, L., Camelbeeck, T., Martin, O., Meynard, C., & Thom, C. (2016). Bimodal pattern
757   of seismicity detected at the ocean margin of an Antarctic ice shelf. *Geophysical Journal*
758   *International*, *206*(2), 1375–1381. https://doi.org/10.1093/gji/ggw214

759   Lombardi, D., Gorodetskaya, I., Barruol, G., & Camelbeeck, T. (2019). Thermally induced icequakes
760   detected on blue ice areas of the East Antarctic ice sheet. *Annals of Glaciology*, *60*(79), 45–
761   56. https://doi.org/10.1017/aog.2019.26

762   Lucas, E. M., Nyblade, A. A., Aster, R. C., Wiens, D. A., Wilson, T. J., Winberry, J. P., & Huerta, A. D.
763   (2023). Tidally Modulated Glacial Seismicity at the Foundation Ice Stream, West Antarctica.
764   *Journal of Geophysical Research: Earth Surface*, e2023JF007172.
765   https://doi.org/10.1029/2023JF007172

766   Minowa, M., Podolskiy, E. A., & Sugiyama, S. (2019). Tide-modulated ice motion and seismicity of a
767   floating glacier tongue in East Antarctica. *Annals of Glaciology*, *60*(79), 57–67.
768   https://doi.org/10.1017/aog.2019.25

769   Mouginot, J., Rignot, E., Gim, Y., Kirchner, D., & Meur, E. L. (2014). Low-frequency radar sounding of
770   ice in East Antarctica and southern Greenland. *Annals of Glaciology*, *55*(67), 138–146.
771   https://doi.org/10.3189/2014AoG67A089

772   Murray, T., Smith, A. M., King, M. A., & Weedon, G. P. (2007). Ice flow modulated by tides at up to
773   annual periods at Rutford Ice Stream, West Antarctica. *Geophysical Research Letters*, *34*(18).
774   https://doi.org/10.1029/2007GL031207

775   Nanni, U., Roux, P., Gimbert, F., & Lecointre, A. (2022). Dynamic Imaging of Glacier Structures at
776   High-Resolution Using Source Localization With a Dense Seismic Array. *Geophysical Research*
777   *Letters*, *49*(6), e2021GL095996. https://doi.org/10.1029/2021GL095996

778   Neave, K. G., & Savage, J. C. (1970). Icequakes on the Athabasca Glacier. *Journal of Geophysical*
779   *Research (1896-1977)*, *75*(8), 1351–1362. https://doi.org/10.1029/JB075i008p01351

780   Nelder, J. A., & Mead, R. (1965). A Simplex Method for Function Minimization. *The Computer Journal*,
781   *7*(4), 308–313. https://doi.org/10.1093/comjnl/7.4.308

782   Osten-Woldenburg, H. V. D. (1990). Icequakes On Ekström Ice Shelf Near Atka Bay, Antarctica.
783   *Journal of Glaciology*, *36*(122), 31–36. https://doi.org/10.3189/S0022143000005517

784   Pattyn, F. (2018). The paradigm shift in Antarctic ice sheet modelling. *Nature Communications*, *9*(1),
785   2728. https://doi.org/10.1038/s41467-018-05003-z

786   Pawlowicz, R., Beardsley, B., & Lentz, S. (2002). Classical tidal harmonic analysis including error
787   estimates in MATLAB using T_TIDE. *Computers & Geosciences*, *28*(8), 929–937.
788   https://doi.org/10.1016/S0098-3004(02)00013-4

789   Pedley, M., Paren, J. G., & Potter, J. R. (1986). The tidal spectrum underneath Antarctic ice shelves.
790   *Journal of Geophysical Research: Oceans*, *91*(C11), 13001–13009.

791   https://doi.org/10.1029/JC091iC11p13001

792   Pirli, M., Hainzl, S., Schweitzer, J., Köhler, A., & Dahm, T. (2018). Localised thickening and grounding

793   of an Antarctic ice shelf from tidal triggering and sizing of cryoseismicity. *Earth and Planetary*

794   *Science Letters*, *503*, 78–87. https://doi.org/10.1016/j.epsl.2018.09.024

795   Podolskiy, E. A., & Walter, F. (2016). Cryoseismology. *Reviews of Geophysics*, *54*(4), 708–758.

796   https://doi.org/10.1002/2016RG000526

797   Podolskiy, E. A., Sugiyama, S., Funk, M., Walter, F., Genco, R., Tsutaki, S., et al. (2016). Tide-

798   modulated ice flow variations drive seismicity near the calving front of Bowdoin Glacier,

799   Greenland. *Geophysical Research Letters*, *43*(5), 2036–2044.

800   https://doi.org/10.1002/2016GL067743

801   Provost, F., Zigone, D., Le Meur, E., Malet, J.-P., & Hibert, C. (2024). Surface dynamics and history of

802   the calving cycle of Astrolabe Glacier (Adélie Coast, Antarctica) derived from satellite

803   imagery. *The Cryosphere*, *18*(7), 3067–3079. https://doi.org/10.5194/tc-18-3067-2024

804   Rack, W., King, M. A., Marsh, O. J., Wild, C. T., & Floricioiu, D. (2017). Analysis of ice shelf flexure and

805   its InSAR representation in the grounding zone of the southern McMurdo Ice Shelf. *The*

806   *Cryosphere*, *11*(6), 2481–2490. https://doi.org/10.5194/tc-11-2481-2017

807   Rignot, E., Mouginot, J., & Scheuchl, B. (2011). Ice Flow of the Antarctic Ice Sheet. *Science*, *333*(6048),

808   1427–1430. https://doi.org/10.1126/science.1208336

809   Rignot, E., Jacobs, S., Mouginot, J., & Scheuchl, B. (2013). Ice-Shelf Melting Around Antarctica.

810   *Science*, *341*(6143), 266–270. https://doi.org/10.1126/science.1235798

811   Rignot, E., Ciracì, E., Scheuchl, B., Tolpekin, V., Wollersheim, M., & Dow, C. (2024). Widespread

812   seawater intrusions beneath the grounded ice of Thwaites Glacier, West Antarctica.

813   *Proceedings of the National Academy of Sciences*, *121*(22), e2404766121.

814   https://doi.org/10.1073/pnas.2404766121

815   RINGS Action Group. (2022). *"RINGS: Collaborative inte rnational effort to map all Antarctic ice-sheet*

816   *margin"* (Scientific Committee on Antarctic Research). Zenodo.

817   https://doi.org/10.5281/zenodo.6638327

818   Röthlisberg, H. (1955). Studies in Glacier Physics on the Penny Ice Cap, Baffin Island, 1953: Part III:

819   Seismic Sounding. *Journal of Glaciology*, *2*(18), 539–552.

820   https://doi.org/10.3189/002214355793702064

821   Röthlisberger, H. (1972). Water Pressure in Intra- and Subglacial Channels. *Journal of Glaciology*,

822   *11*(62), 177–203. https://doi.org/10.3189/S0022143000022188

823   Schoof, C. (2007). Ice sheet grounding line dynamics: Steady states, stability, and hysteresis. *Journal*

824   *of Geophysical Research: Earth Surface*, *112*(F3). https://doi.org/10.1029/2006JF000664

825   Stutzmann, E., Schimmel, M., Patau, G., & Maggi, A. (2009). Global climate imprint on seismic noise.

826   *Geochemistry, Geophysics, Geosystems*, *10*(11), 2009GC002619.

827   https://doi.org/10.1029/2009GC002619

828 Weertman, J. (1957). On the Sliding of Glaciers. *Journal of Glaciology*, *3*(21), 33–38.

829   https://doi.org/10.3189/S0022143000024709

830 Winberry, J., Anandakrishnan, S., Wiens, D. A., & Alley, R. B. (2013). Nucleation and seismic tremor

831   associated with the glacial earthquakes of Whillans Ice Stream, Antarctica. *Geophysical*

832   *Research Letters*, *40*(2), 312–315. https://doi.org/10.1002/grl.50130

833 Zoet, L. K., Anandakrishnan, S., Alley, R. B., Nyblade, A. A., & Wiens, D. A. (2012). Motion of an

834   Antarctic glacier by repeated tidally modulated earthquakes. *Nature Geoscience*, *5*(9), 623–

835   626. https://doi.org/10.1038/ngeo1555

836

837 **References From the Supporting Information:**

838 Andrews, L. C., Catania, G. A., Hoffman, M. J., Gulley, J. D., Lüthi, M. P., Ryser, C., et al. (2014). Direct

839   observations of evolving subglacial drainage beneath the Greenland Ice Sheet. *Nature*,

840   *514*(7520), 80–83. https://doi.org/10.1038/nature13796

841 Bartholomew, I., Nienow, P., Sole, A., Mair, D., Cowton, T., & King, M. A. (2012). Short-term

842   variability in Greenland Ice Sheet motion forced by time-varying meltwater drainage:

843   Implications for the relationship between subglacial drainage system behavior and ice velocity.

844   *Journal of Geophysical Research: Earth Surface*, *117*(F3). https://doi.org/10.1029/2011JF002220

845 Chen, G. (1999). *GPS kinematic positioning for the airborne laser altimetry at Long Valley, California*

846   (Thesis). Massachusetts Institute of Technology. Retrieved from

847   https://dspace.mit.edu/handle/1721.1/9680

848 Herring, T. A., King, R. W., Floyd, M. A., & McClusky, S. C. (2018). Introduction to GAMIT/GLOBK,

849   *Massachusetts Institute of Technology*.